ASME Journal of Manufacturing Science and Engineering
Online journal at:
https://asmedigitalcollection.asme.org/manufacturingscience

Fatigue Scattering Analytics and Prediction of SS 316L Fabricated by Laser Powder Bed Fusion

Panayiotis Kousoulas
Department of Mechanical and Aerospace Engineering,
Rutgers University-New Brunswick,
Piscataway, NJ 08854;
New Jersey Advanced Manufacturing Initiative,
Rutgers University-New Brunswick,
Piscataway, NJ 08854
e-mail: pk538@scarletmail.rutgers.edu

Y. B. Guo[1]
Department of Mechanical and Aerospace Engineering,
Rutgers University-New Brunswick,
Piscataway, NJ 08854;
New Jersey Advanced Manufacturing Initiative,
Rutgers University-New Brunswick,
Piscataway, NJ 08854
e-mail: yuebin.guo@rutgers.edu

Laser powder bed fusion (LPBF) is an enabling process manufacture of complex metal components. However, LPBF is prone to generate geometrical defects (e.g., porosity, lack of fusion), which causes a significant fatigue scattering. However, LPBF fatigue scattering data and analysis in the literature are not only sparse and limited to tension-compression mode but also inconsistent. This article presents a robust high-frequency fatigue testing method to construct stress-cycle curves of SS 316L to understand the scattering nature and predict the scattering pattern. A series of bending fatigue tests are performed at different stress amplitudes. Two different runout criteria are used to investigate fatigue life, fatigue limits, and scattering. The endurance limit reaches around 300 MPa for the defect size distribution at the selected process space. The defect size-based fatigue limit model is found to underestimate the endurance limit by about 30 MPa when comparing with the experimental data. Fatigue scattering is further calculated by using 95% prediction intervals, showing that low fatigue scattering is present at high stresses while a large variation of fatigue life occurs at stresses near the knee point. [DOI: 10.1115/1.4066803]

Keywords: laser powder bed fusion, fatigue scattering, endurance limit, fatigue testing, SS 316l, additive manufacturing

1 Introduction

Laser powder bed fusion (LPBF) is one of the major metal additive manufacturing (AM) processes, which uses a laser heat source to fuse metal powders in successive layers to create a 3D part. Compared to traditional manufacturing processes (e.g., machining, forging), LPBF offers an opportunity for making complex metal components with design freedom, short development time, and environmental sustainability. However, the LPBF-fabricated components often suffer from severe fatigue scattering problems, i.e., the fatigue life of a component produced by LPBF under similar process conditions exhibits a very large variation [1,2]. There is a consensus within the AM community that fatigue scattering imposes a significant challenge to using an LPBF process for fabricating load-bearing and highly reliable components. This significantly limits the applicability of LPBF processes. Fatigue scattering of LPBF parts is induced by geometrical defects, such as gas pores and lack-of-fusion (LOF) distributed throughout a printed part, which reduce material strength and make it challenging to merit applications in high-reliability situations [3,4]. While researchers are trying to reduce the magnitude and prevalence of these defects through developing an optimal process map [5], or leveraging in situ monitoring for closed-loop control [6,7], it is impossible to fully eliminate them since these random defects are inherent to the LPBF process. The inherent fatigue scattering must therefore be quantified to assess the LPBF part quality. It is especially relevant to consider the scattering about the endurance limit S_e, also known as the fatigue limit, since this stress value is the theoretical limit for safe stresses in the component design.

Since identical part geometries may have different defect distributions, a batch of parts cannot be expected to have uniform quality. Therefore, it is essential to characterize the lowest expected fatigue performance for a batch of parts and relate this conservative quality measure to the defect distribution generated by a given print job. Murakami proposed a mechanics-based model for the fatigue limit σ_w of metallic materials based on defect size $\sqrt{\text{area}}$, measured by the square root of the projected defect area on the plane normal to the applied stress [8,9]. This semi-empirical model (referred to as the $\sqrt{\text{area}}$ model) was derived for high-strength steels with Vickers hardness HV > 400 based on the origin of fracture for high-strength steels occurring at surface and interior defects [10,11]. The defect location relative to the material surface (e.g., surface versus interior) determines the material constant C. The $\sqrt{\text{area}}$ model can be applied to metal AM materials by using statistics of extremes of defect sizes measured from a specimen to predict a maximum defect size $\sqrt{\text{area}_{\max}}$ [12]. Murakami's predicted fatigue limit σ_w can thus estimate the lower bound of the scatter band of fatigue strength of LPBF materials, which is important for quantifying both the reliability of the material and its uncertainty. A more recent study by Murakami et al. [1] normalized *S-N* data, σ/σ_w versus N, to analyze the essential structure of *S-N* curves and to check the validity of the original *S-N* data. The net amount of the stress above the predicted fatigue limit ($\sigma/\sigma_w > 1$), rather than the absolute value of the applied stress σ, determines the fatigue

[1]Corresponding author.

Manuscript received July 3, 2024; final manuscript received September 30, 2024; published online October 24, 2024. Assoc. Editor: Vincent Wagner.

Table 1 Runout stresses of IPBFed SS 316L from the literature

Energy density (J/mm^3)	Loading direction with respect to buildup direction	Surface finishing method	Heat treatment	Load ratio R	Loading method	Cycles to runout	# Runouts	Runout stress (MPa)	Ref.
100	Perpendicular	Grinding	No	0.1	Axial	1×10^6	2	350	[13]
36	Parallel	Polishing	Yes	0.1	Axial	4×10^6	1	250	[2]
100	Parallel	Polishing	Yes	0.1	Axial	4×10^6	2	300	
				−1	Rotating bending	4×10^6	3	350	
65	Parallel	Polishing	Yes	−1	Axial	1×10^7	1	260	[14]
56	Parallel	Turning	Yes	−1	Axial	2×10^7	1	300	[15]
60	Perpendicular	Polishing	No	0.1	Axial	NA	NA	180	[16]

crack growth rate. The scattering of *S-N* data of AM materials can be predicted by this analysis in combination with the statistics of extremes of defect sizes.

However, LPBF fatigue studies in the literature are not consistent in terms of the number of data points and the runout criteria used to obtain an *S-N* curve. This raises questions about the statistical significance of the results, especially when quantifying the distribution of the fatigue life. It also creates a possibility to overpredict or underpredict the true endurance limit S_e, which can either lead to unsafe designs or loss of profits by being overconservative. Table 1 depicts experimental runout stresses (i.e., not necessarily the actual endurance limits) for LPBFed SS 316L under different runout criteria retrieved from the literature, as well as comparative information on the material manufacturing and preparation procedures for these fatigue studies. The inconsistency in the stress values is clear to see regardless of whether the comparison is of stress ratio, runout criterion, or number of runouts obtained. The last row of Table 1 is included for the comparison of how the endurance limit is obtained. All studies referenced used *S-N* curves except the last study, which used a thermographic method to detect the stress level at which fatigue damage was instantiated. While the theory of this method appears sound, it is suspected to underestimate S_e for stricter runout criteria ($\geq 10^7$ cycles) [17]. This definitely seems to be the case when compared to the much higher values given by traditional *S-N* curves.

While traditional metal manufacturing methods have well-established material standards [18], LPBF standards are still in their infancy [19,20]. For example, ASTM standard F2924 was originally approved in 2012 to guide metal AM manufacturers and customers for only supplying and ordering AM parts, leaving the determination of acceptable part quality (e.g., mechanical properties, allowable porosity) up to the agreement of the supplier and purchaser [21]. Thus, there is clearly a need for standard methods of quantifying scatter in part quality, especially for fatigue performance in industrial settings or critical applications.

The objectives of this work are as follows: (1) A *S-N* curve for LPBFed SS 316L is created to capture the statistical scatter in the fatigue life at different stress amplitudes σ_a. (2) The fatigue scattering is quantified by using 95% prediction intervals for the lower and upper bound finite fatigue life. (3) The experimental *S-N* curve is normalized using Murakami's lower bound fatigue strength (i.e., $\sqrt{\text{area}}$ model) to compare the prediction to the experimentally found endurance limit. Figure 1 depicts the overall experimental procedure from a high-level perspective. Each step of the procedure is discussed in detail in the following sections.

2 Preparation and Characterization of Fatigue Samples

A block of SS 316L material is made by LPBF, from which fatigue samples and microstructure samples are extracted by wire-electrical discharge machining (EDM). Microstructure samples are polished and etched to reveal the grain morphology under an optical microscope. Dog-bone fatigue samples are polished

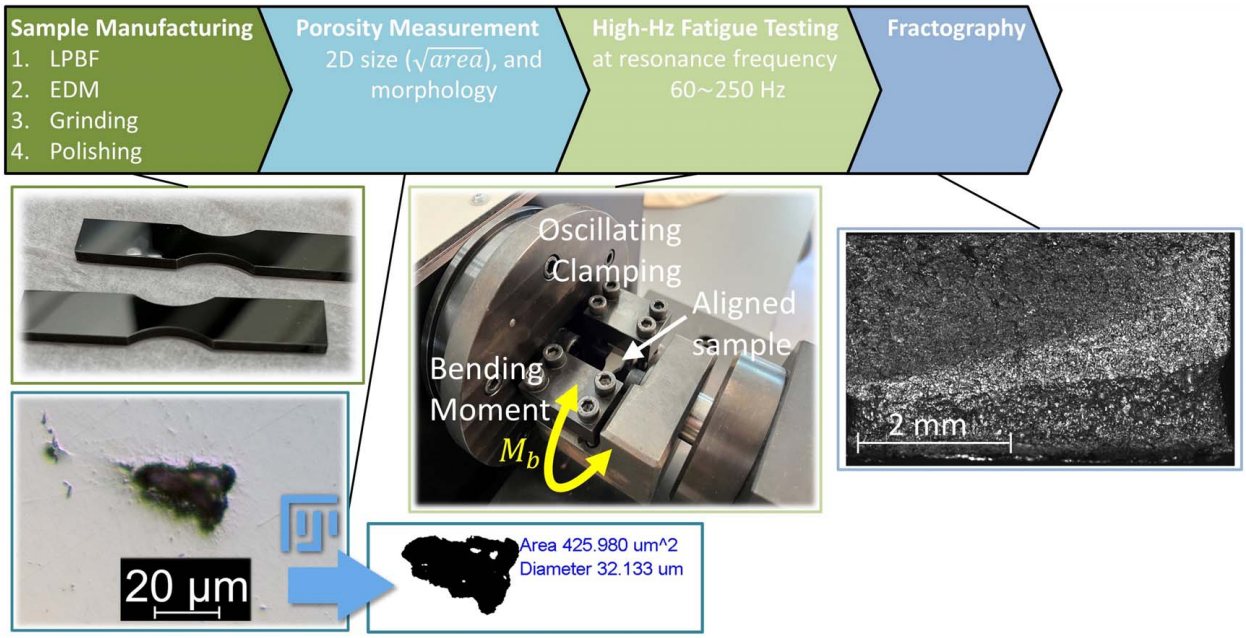

Fig. 1 Overview of experimental procedure

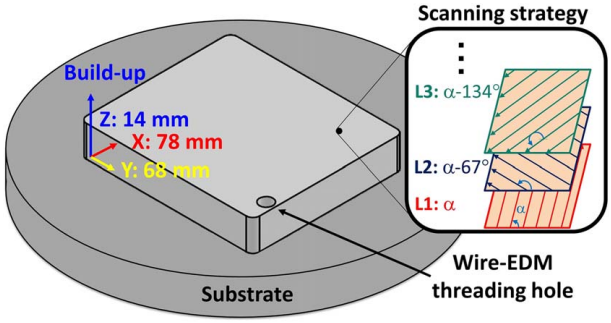

Fig. 2 Bulk sample geometry and scanning strategy

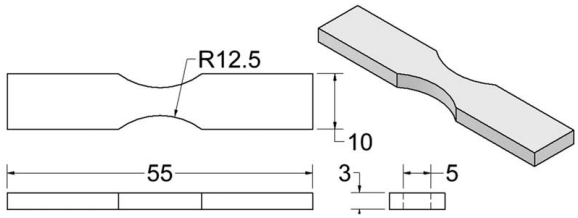

Fig. 3 Dog-bone fatigue sample geometry with dimensions in mm

to remove the heat-affected zones induced by EDM and improve surface finish. The hardness and geometrical defects in the gauge section of the samples are recorded prior to fatigue testing.

2.1 LPBF of Bulk Material SS 316L. An AconityMINI LPBF machine was used to fabricate the block (Fig. 2) of SS 316L material. The SS 316L powder composition is presented in Table 2. The LPBF parameters are presented in Table 3. These parameters were selected by experience to minimize the size of any LOF geometrical defects formed during printing. The print job was optimized using Netfabb® Simulation Utility to achieve minimal thermal deformation during the printing process. The bulk geometry was printed on top of 1 mm tall cylindrical supports to reduce the warping of the substrate. The filleted corners were also used to reduce deformation, which is especially prevalent in the first few layers of printing. A hole was printed to allow for wire threading during EDM preparation of the fatigue samples. The wire-EDM procedure involves a two-step machining operation. First, a slicing operation is performed by sectioning 14 dog-bone samples inside the bulk material. Then the profiles of the dog-bone samples are machined simultaneously by machining with the bulk sample oriented by a 90 deg counterclockwise rotation about its *y*-axis (see Fig. 2). This procedure is explained in greater detail in the previous work [22].

2.2 Fatigue Sample Preparation and Characterization. The geometry of the 14 dog-bone fatigue samples is shown in Fig. 3. A LECO PX300 polisher was used to grind the sample surfaces with abrasive papers (240, 320, 600, 1200 grit), followed by polishing with diamond suspensions (3 μm, 1 μm). The areal surface roughness (S_a) as well as the average surface roughness (R_a) (in both horizontal and vertical directions, $R_{a,h}$ and $R_{a,v}$, respectively) were measured on the sample gauge sections using a Zeiss LSM 900 laser confocal microscope. The average roughness values were approximately $S_a = 0.35$ μm, $R_{a,h} = 0.14$ μm, and $R_{a,v} = 0.16$ μm. Vickers hardness testing was conducted with a LECO LV-100 with a diamond tip indenter. A 10 kg load F with a 10-s dwell time was applied for each indent. Each indent location was checked to be defect free and separated by at least 2 mm from other indents to avoid interference. A Keyence VR-3100 optical microscope was used to measure the indentation diagonal lengths d_1 and d_2 in mm to calculate the Vickers hardness number:

$$\mathrm{HV} = \frac{1.8544 \times F}{d_1 d_2} \tag{1}$$

with the average and sample standard deviation of the hardness values being $\mathrm{HV} = 243 \pm 7 \left[\frac{\mathrm{kgf}}{\mathrm{mm}^2}\right]$.

A sampling of the geometrical defects of the printed SS 316L block was recorded from the gauge sections of six of the polished samples. The gauge sections were manually scanned for defects at least 10 μm in diameter using the LSM 900 microscope. Each resolved defect was photographed for automatic measurement in ImageJ. A custom macro was created to measure the area and Feret caliper (FC) diameter of the photographed defects. While the defect area measurement has been popularized by Murakami, the FC diameter metric gives a more practical description of physical defect size. Thus, both measurement metrics were used for further comparison. Since the black-and-white pixel intensities (0–255) were used to detect defects in the photos, the macro was iterated three times with increasing minimum intensity threshold settings (75, 88, and 100). Since the average defect size increased by about 1.5% and the number of detected defects increased by about 15% for each increase in the minimum threshold intensity value, the middle ground was chosen by using the defect sizes measured using the minimum threshold intensity value of 88.

The distribution in FC diameter size as well as the correlation between the square root of the defect area ($\sqrt{\text{area}}$) and the FC diameter (d) sizes are both shown in Fig. 4. Since a total of 441 defects were measured, this was sufficient for capturing the overall trend in the total population of defects, as shown in the previous study [23]. Thus, only six samples were inspected for geometrical defects.

Statistics of extremes were applied using the Gumbel, gamma, Weibull, and lognormal cumulative distribution functions (CDFs) to predict the maximum defect size at 99.9% probability for both size metrics $\sqrt{\text{area}}$ and d. As shown in a previous study, it is important to compare several different CDFs to have the best fit to the defect dataset as well as a realistic predicted maximum (i.e., larger than the measured maximum by ~15–20%) [24]. In this case, the Weibull CDF with a shape parameter $\gamma = 0.6$ gave the best linear extrapolation of the maximum size, with the extrapolations shown in Fig. 5.

Table 3 LPBF process parameters

Parameter	Value	Units
Layer thickness	0.030	mm
Hatch spacing	0.080	mm
Laser speed	800	mm/s
Laser power	120	W
Scan vector rotation	67 deg	Per layer
Stripe hatch width	1	cm

Table 2 SS 316L powder chemical composition

C	Cr	Fe	Mn	Mo	Ni	P	Si	S
0–0.03%	16–18%	61.89–72%	0–2%	2–3%	10–14%	0–0.045%	0–1%	0–0.03%

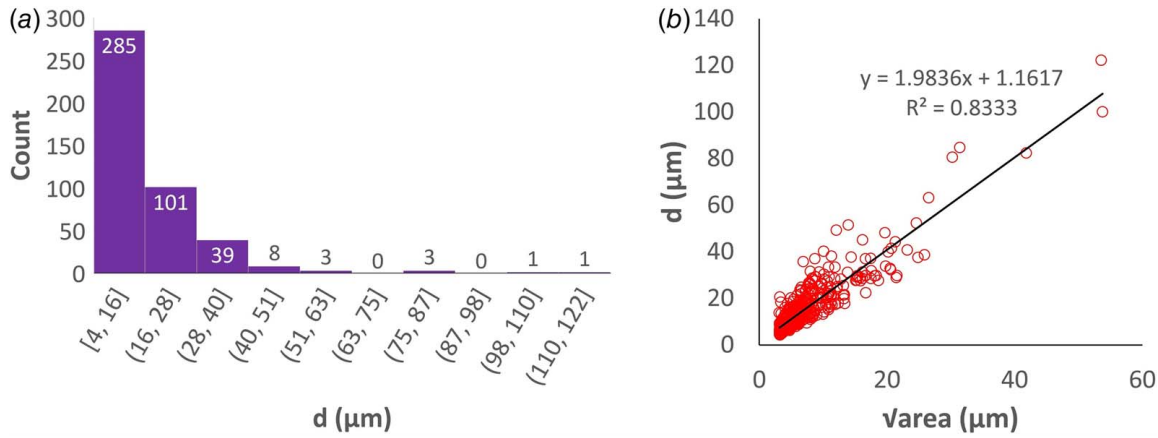

Fig. 4 (*a*) Measured defect size distribution and (*b*) correlation of defect size metrics

2.3 Microstructure Etching and Optical Imaging. Sections were taken from the LPBFed block to observe microstructures (Fig. 6) perpendicular to and parallel to the build direction. The samples were polished using the same procedure as for the fatigue samples, with the addition of a final polish with 0.1 μm silica. Vilella's etchant (100 mL 95% ethanol, 5 mL 37% HCl, 1 g picric acid) was swabbed on the polished samples for several minutes until the originally highly reflective surfaces turned hazy. Optical images taken with the LSM 900 microscope of the etched microstructures are displayed in Fig. 6. At higher magnification, the melt pool boundaries became visible as white lines with brightfield imaging. While the grain boundaries were also visible using brightfield imaging, darkfield illumination was also used to highlight nonflat surface features (e.g., porosity, grain boundaries, scratches). In the ZX plane (parallel to the build direction), columnar grains are visible, whereas in the YX plane (perpendicular to the build direction), uniform circular grains are evenly oriented, which is the expected microstructure of as-printed LPBF metals [25]. As a sanity check, the scanning strategy of 67 deg rotation between layers can be checked by finding the angle between noncolinear scanning paths, as shown in the YX micrograph of Fig. 6.

3 Fatigue Testing

Fully reversed bending fatigue testing was conducted at resonance frequency to achieve high-cycle fatigue as well as to track the fatigue process. A RUMUL Cracktronic resonance testing machine and associated software were used to conduct the experiment. The fatigue loading (i.e., stress amplitude and mean stress) was applied at a frequency equal to the resonant frequency of the mounted sample. This not only enables the monitoring of crack initiation and propagation through the recorded changes in frequency but also allows for much higher testing frequencies than conventional fatigue machines. Pure bending is applied to a mounted dog-bone sample by fixing one end of the sample and oscillating the other end. The sample was precisely aligned to ensure pure bending with respect to the sample longitudinal center through custom-made shims. This consistently orients the sample for each test. The oscillation frequency is kept at the system resonance frequency by closed-loop control. The frequency at the start of a fatigue test is used as a reference value, which was about 62 Hz for the LPBFed SS 316L samples in this study. As cracks grow inside the sample, the frequency reduces from the reference value. The drop in frequency is used to monitor the extent of damage in the sample where the failure criterion of $-\Delta 2$ Hz stops the test. In this way, the test is concluded prior to gross fracture and gives more insight into the fatigue process (e.g., cycles to crack initiation and propagation) than the standard practice of simply recording the number of cycles to gross fracture. Using the fatigue criterion of $\Delta 2$ Hz frequency drop for all samples makes the fatigue results comparable [22].

Two different runout criteria are used to compare the differences in experimental endurance limits obtained by runout data points. Initially, the runout criterion is set to 1×10^7 cycles, which is a good middle ground between more relaxed requirements of around 1×10^6 cycles and highly strict standards of 1×10^9 cycles. This first runout criterion enables test data to be compiled into an initial *S-N* curve. Once the endurance limit of the initial curve is determined by previous runouts, additional testing under

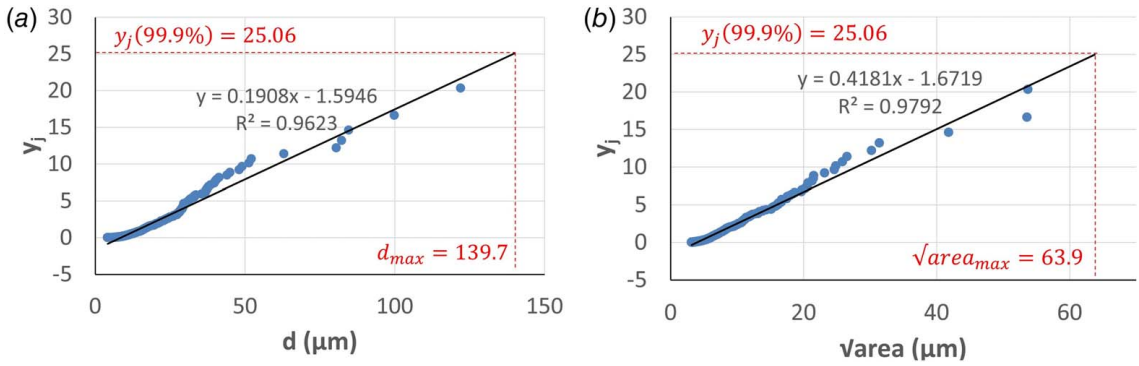

Fig. 5 Extrapolated maximum defect sizes for (*a*) FC diameter *d* and (*b*) $\sqrt{\text{area}}$ using the Weibull CDF, whose inverse $y_j = [-\ln(1 - F_j)]^{\frac{1}{\gamma}}$ is a function of the probability F_j of defect with ranked size $j = 1, \ldots, n$ being the largest defect in existence for *n* measured defects

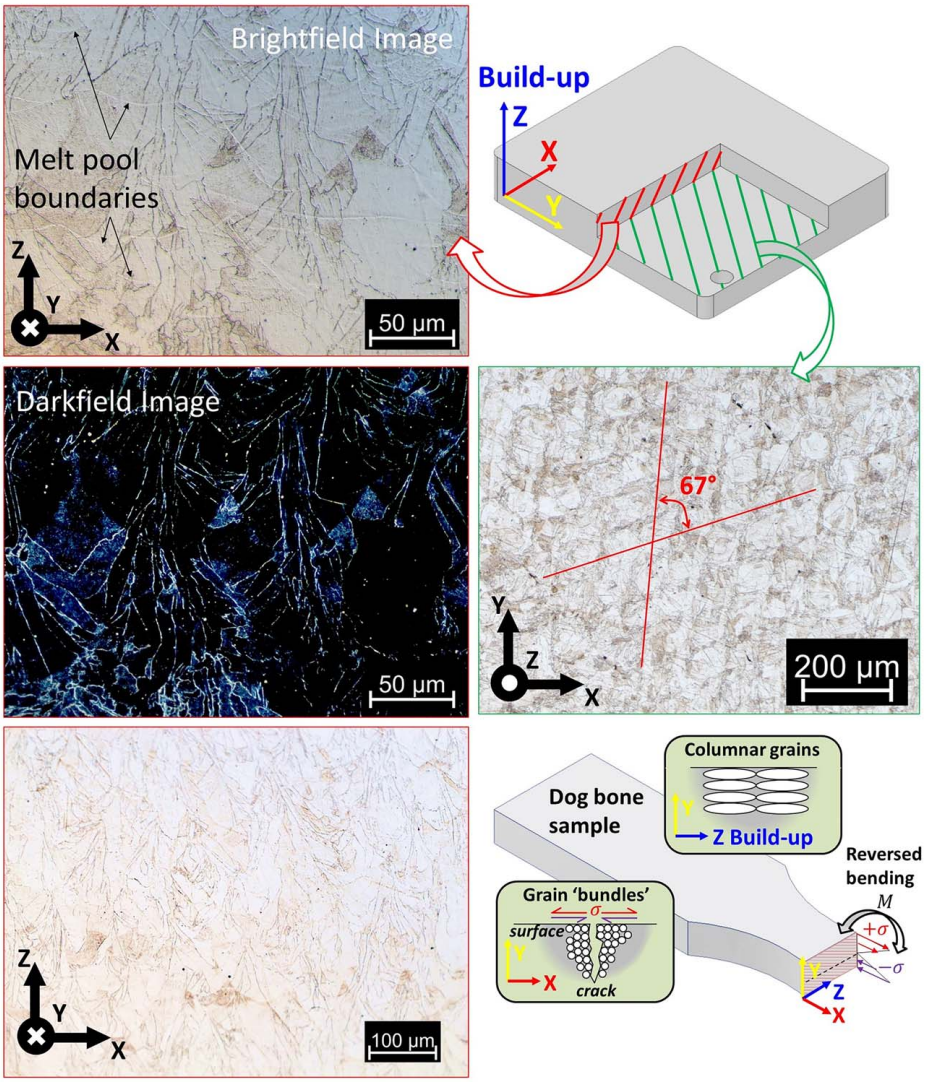

Fig. 6 Brightfield and darkfield images of etched microstructure at multiple magnifications. Columnar grains align with the buildup direction and are perpendicular to the applied loading.

a second stricter runout criterion of 2×10^7 cycles is conducted to verify or update the endurance limit. By using Murakami's normalization method, the normalized *S-N* curves are created using both the size metrics $\sqrt{\text{area}}$ and d for comparison of the predicted normalized stress σ/σ_w. In this way, the experimental endurance limit can be compared to the prediction given by both size metrics.

After determining the endurance limit, select load levels are retested to increase the number of data points in the finite life region of the *S-N* curve. This helps to quantify the statistical scatter in fatigue life more confidently.

4 Results and Discussion

Of the 14 fatigue samples tested, 9 samples were fatigued and 5 samples reached the runout criteria (3 samples at 1×10^7, 2 samples at 2×10^7). A representative fractured surface is shown in Fig. 7. Since the fatigue failure criterion during testing prevents the fatigue process from reaching total fracture, the fatigue crack only propagates partially through the sample (gauge) cross section. To reveal the fracture surface, fatigued samples are manually pried open, as is done in practice to inspect fracture surfaces of cracked samples. Figure 7 exemplifies the characteristic pattern of all

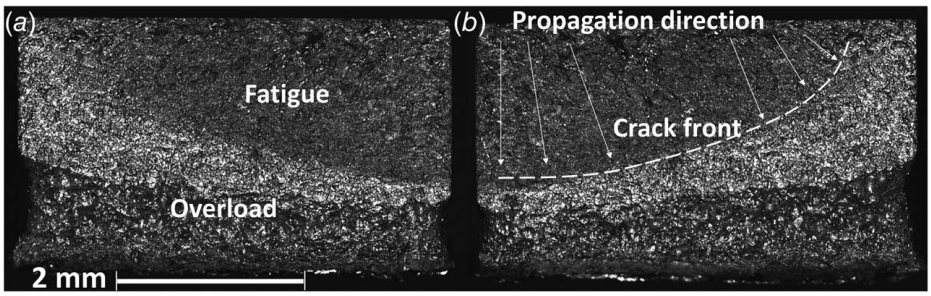

Fig. 7 Fracture surface for sample with $\sigma_a = 345$ MPa and $N = 1.45 \times 10^6$ cycles with (*a*) dog-bone sample half A and (*b*) half B, displayed side by side

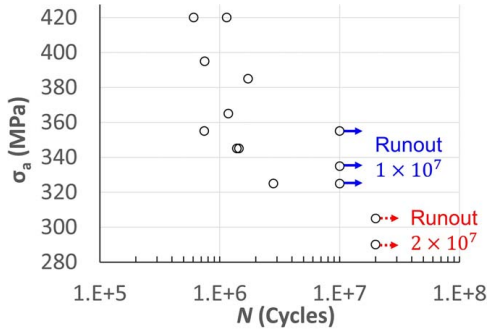

Fig. 8 Experimental *S-N* curve of LPBFed SS 316L with two runout criteria

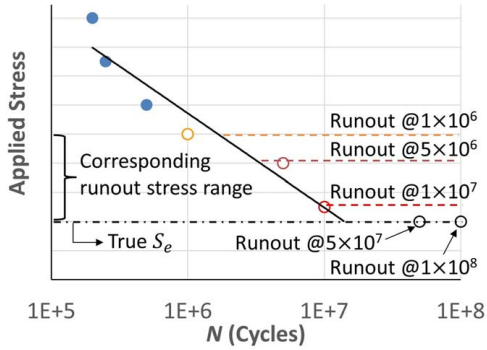

Fig. 9 Schematic of the difference between runout stresses and the true endurance limit S_e

fractured sample surfaces. The crack initiation sites cannot be exactly identified; nevertheless, fatigue seems to originate from porosity near the sample surfaces.

4.1 Experimental Construction of *S-N* Curves. The *S-N* curve is shown in Fig. 8, and the tabular data are presented in Table 4. It is interesting to note the scatter in the endurance limit for the runout criterion of 1×10^7, which spans from 325 to 355 MPa. These stress levels gave mixed results, with one runout and one fatigue failure occurring at both 325 and 355 MPa stress amplitudes. Not only this, but the fatigued sample at the stress amplitude of 355 MPa failed before reaching 1×10^6 cycles, which is more than an order of magnitude earlier than its runout counterpart. Of the seven samples tested in the range of 325–355 MPa, four failed and three reached runout. If the test plan for determining the endurance limit stopped after one or even two runouts (at different load levels) without retesting, the results would not have captured the inherent scatter.

S_e is *not* the stress level at which runout occurs. When a runout criterion is used in fatigue studies, it stops fatigue tests from running without the apparent end. However, the true definition of S_e, as stated by Murakami and Beretta, is the threshold stress below which fatigue cracks do not propagate [26]. Thus, S_e is dependent on microstructural strength as well as the upper bound of the defect size distribution, which characterizes the defects expected to cause crack propagation. Just because a fatigue sample reaches the prescribed runout criterion, it does not mean that the stress it experienced is at the endurance limit (see Fig. 9). Assuming a batch of samples has equivalent microstructures, the difference in critical defect sizes will be the cause of failure in some samples and the achievement of runout in other samples at the same applied stress. If the runout criterion is carefully chosen, the loading applied for runout samples will be near S_e. The scatter in S_e is evident for the runout condition of 1×10^7 cycles since both runouts and failures were achieved over a range of 30 MPa. This shows that a stricter runout condition is needed to estimate S_e with less ambiguity, which is the case for the runout condition of 2×10^7 cycles. This technique can be adopted in practice for fatigue testing of AM materials to better understand the scattering nature near the endurance limit.

It is understandable that fatigue testing is costly due to raw material costs, laborious sample preparation, and long testing times. Yet, this should not excuse sparse testing of such a critical material property. This especially holds true for AM materials, which are known to exhibit large fatigue scattering. Mower and Long conducted rotating-bending fatigue tests on conventional wrought and LPBFed SS 316L samples [27]. Only five wrought samples were used to generate an *S-N* curve since a steady decline in applied stress resulted in a predictable increase in fatigue life. However, the LPBF fatigue test results did not follow the expected fatigue relationship and rather exhibited an upper and lower bound distribution of stress values at different fatigue lives. This distribution was quantified in another study where, for a fixed load level and the given LPBF process conditions, multiple fatigue tests gave a large range of cycles to failure ($\sim 10^3$–10^4) [22]. More dismal is the fact that test specimens at lower load levels cannot be expected to outlast those at higher load levels. This fatigue scattering is due to the random geometrical defects created during the LPBF process, which act as stress concentrations and crack initiators [28,29]. Since identical part geometries may have different defect distributions, a batch of parts cannot be expected to have uniform quality. Therefore, it is essential to characterize the lowest expected fatigue performance for a batch of parts and relate this conservative quality measure to the defect distribution generated by a given print job.

For a more confident assessment of S_e, the longer runout criterion of 2×10^7 gives a stress range of 290–305 MPa, which agrees well with *S-N* data from the literature (see Table 1). Of course, this experimental method could be taken to the extreme, where even more testing could be conducted at longer and longer runout criteria. A reasonable tradeoff must be achieved between cost and confidence. The method shown in this study reaches this tradeoff by heavily testing at a dependable runout criterion (i.e., not too weak and not too extreme), and testing lightly at a stricter runout criterion to capture the scattering in the expected operating conditions and provide a more confident endurance limit when permissible by design. This may not be feasible for very high-cycle fatigue applications that require extreme runout criteria (e.g., 1×10^9 cycles) depending on the testing time.

Even with rigorous experimentation, it is still possible for failure to occur near or below the experimental endurance limit due to the random defects that are generated in LPBF. Thus, it is helpful to find the predicted lower-bound endurance limit for a given extreme defect size. Murakami's prediction of the lower-bound endurance limit

$$\sigma_w = C(\mathrm{HV} + 120)/(\sqrt{\mathrm{area}})^{1/6} \tag{2}$$

Table 4 Fatigue testing data

Stress amplitude (σ_a) (MPa)	290	305	325	335	345	355	365	385	395	420
Cycles (N) $\times 10^6$	20.00	20.00	2.81 10.00	10.00	1.45 1.39	0.74 10.00	1.18	1.73	0.75	0.61 1.14

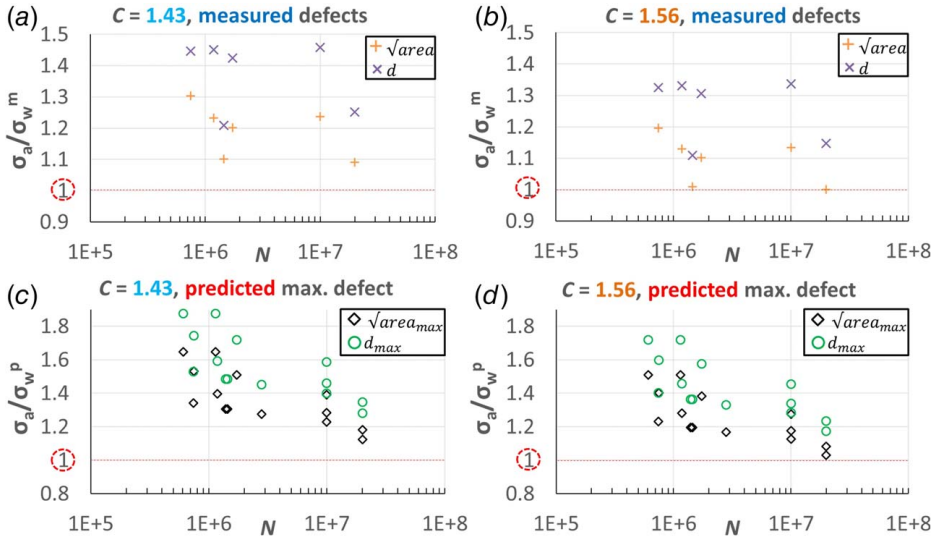

Fig. 10 Analysis of endurance limit using Murakami's normalized stress with defect location constant *C* varied for internal (1.43) and surface (1.56) defects. σ_w^m is calculated from measured maximum defect sizes from each of the six inspected samples and σ_w^p is calculated from the predicted maximum defect size.

can be found by using the maximum predicted defect size with $C = 1.43$ (signifying a surface defect, which is the most detrimental case) and the average HV measured. This gives $\sigma_w = 259$ (MPa) for $\sqrt{\text{area}}_{\max}$ and $\sigma_w = 228$ (MPa) for $d_{\max}$. These values underpredict the experimental endurance limit by a large margin (at minimum about 30 MPa), especially when using the FC diameter metric for defect size. If $C = 1.56$ is used in Eq. (2) instead (signifying an internal defect), $\sigma_w = 283$ (MPa) for $\sqrt{\text{area}}_{\max}$ and $\sigma_w = 248$ (MPa) for $d_{\max}$, which is closer to the experimental endurance limit and may provide a less conservative estimate than the previous calculation using the surface defect location constant value. Equation (2) was not derived for the FC diameter size metric, which is inherently larger than the $\sqrt{\text{area}}$ size metric. For a perfectly circular defect with radius r, $d = 2r$, while $\sqrt{\text{area}} = r\sqrt{\pi} \approx 1.772r$. If $\frac{\sqrt{\pi}}{2} \times d$ is used in Eq. (2), the values only increase by 2% and still do not equate to the values found using $\sqrt{\text{area}}$. A better conversion of large defect sizes between $\sqrt{\text{area}}$ and d size metrics is the linear regression from the correlation plot of size metrics in Fig. 4.

4.2 Defect Size-Based Prediction of *S-N* Curves. Four different normalized *S-N* curves, σ/σ_w versus N, are shown in Fig. 10. These curves illustrate how closely the predictions agree with the experimental endurance limit. To explore different uses of Eq. (2) for calculating σ_w, three parameters are varied: (1) the defect size metrics ($\sqrt{\text{area}}$ and d), (2) the *measured* maximum as well as the *predicted* maximum defect size values (giving σ_w^m for measured and σ_w^p for predicted), and (3) the defect location constant C is alternated between surface and internal cases. For the cases using the measured defect sizes (Figs. 10(*a*) and 10(*b*)), the maximum measured defect size is used in Eq. (2) to normalize the stress amplitude σ_a. Since defect sizes were only measured from six samples, only six data points per size metric are shown in these plots. For Figs. 10(*c*) and 10(*d*), the maximum predicted defect sizes are constant and are applied to the normalization of every data point's stress. The general trend shows that the defect location constant has the greatest impact on the value of σ_w. This makes sense, given that C is a linear factor in Eq. (2), while the effect of defect size is restricted by the fractional exponent acting upon it and by the small (~15–20%) difference in maximum measured versus predicted defect size.

4.3 Prediction of Fatigue Scattering. This section aims to predict the scattering bands of the finite life region of the *S-N* curve. The ordinary least-squares method is first used to obtain a linear fit for the logarithmic finite life curve:

$$y = mx + b \tag{3}$$

(i.e., $y = \log_{10} N$ and $x = \log_{10} \sigma$, with $\sigma = \sigma_a$). The slope and intercept are given by

$$m = \frac{\sum_i (x_i - \bar{x})(y_i - \bar{y})}{\sum_i (x_i - \bar{x})^2} \tag{4}$$

and

$$b = \bar{y} - m\bar{x} \tag{5}$$

for mean values $\bar{x}$ and $\bar{y}$. The linear regression represents the population mean value of the logarithmic fatigue life at a given logarithmic stress amplitude. It is important to check the assumptions of linear regression are satisfied. Two test conditions are used, the first being that the residual errors of the regression,

$$r_i = (\log_{10} \text{N}_i)_{\text{regression}} - (\log_{10} \text{N}_i)_{\text{experimental}} \tag{6}$$

are distributed in a horizontal band that is centered and symmetric about the x-axis. The second test condition (homoscedasticity) requires a linear normal probability plot of the residuals, where

$$z_i = \frac{r_i - \mu}{\varsigma} \tag{7}$$

is the z-score of a given residual, which shifts and normalizes the value by the sample mean μ and sample standard deviation ς of the residuals, respectively.

The upper and lower bound fatigue life (N^u and N^l) with respect to the fitted regression line can be calculated using a two-sided prediction interval [30]

$$\log_{10} N = m \times \log_{10} \sigma + b \pm I(\log_{10} \sigma) \tag{8}$$

The interval I is given by

$$I = t_{\alpha/2,\nu} \cdot \varsigma_e \sqrt{1 + \frac{1}{k} + \frac{(\log_{10}\sigma - \overline{\log_{10}\sigma})^2}{\sum_i (\log_{10}\sigma_i - \overline{\log_{10}\sigma})^2}} \tag{9}$$

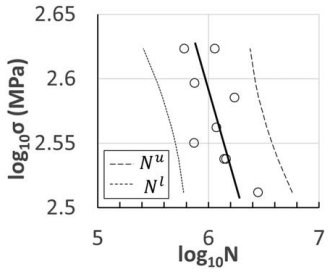

Fig. 11 Upper and lower bounds of fatigue life at 95% probability with respect to the regression line of the finite life log-log *S-N* curve.

Table 5 Prediction interval data

Stress amplitude (σ_a) (MPa)	Cycles (N) $\times 10^6$	N^l $\times 10^6$	N^u $\times 10^6$
325	2.81	0.60	5.72
345	1.39 1.45	0.54	4.25
355	0.74	0.50	3.75
365	1.18	0.47	3.37
385	1.73	0.39	2.84
395	0.75	0.35	2.66
420	0.61 1.14	0.26	2.38

with the inverse Student's t-distribution value t as a function of probability $\alpha/2$ and degrees-of-freedom $\nu = k - 2$ for k samples (i.e., number of nonrunout data points), and the standard error of the estimate

$$\varsigma_e = \sqrt{\frac{\sum_i (\log_{10}\mathrm{N}_i - \overline{\log_{10}\mathrm{N}})^2}{k-2}} \tag{10}$$

All terms in Eq. (9) are constant except for the $\log_{10}\sigma$ term in the radical, which makes Eq. (8) only a function of the logarithmic stress. For a probability of 95%, the significance level $\alpha = 1 - 0.95 = 0.05$, which is the value chosen for this study.

The 95% prediction intervals for the fatigue life in the finite life region of the *S-N* curve are shown in Fig. 11, and the prediction interval data (upper and lower fatigue lives N^u and N^l, respectively) are given in Table 5. Since logarithmic stress and cycle values were used, the upper bound fatigue life values are much further from the regression line than the lower bound fatigue lives, as shown in Fig. 12. Since the lower bound curve is more critical for fatigue design, the upper bound curve is not of major concern. However, it is interesting to see in Fig. 12 that larger applied stresses result in statistically less scatter in the fatigue life in the finite life region. This agrees with the earlier observation of the high amount of scatter around the stress range of 325–355 MPa. This can be understood to mean that at larger stress levels crack propagation is steadier and more predictable than at lower stresses, where the random distribution of defects has more influence on when cracks initiate due to the greater impact of stress concentrations. That is why it is most important to carefully capture the knee point and to use multiple runout conditions during fatigue testing of LPBF materials to dutifully capture the scattering at low-stress levels.

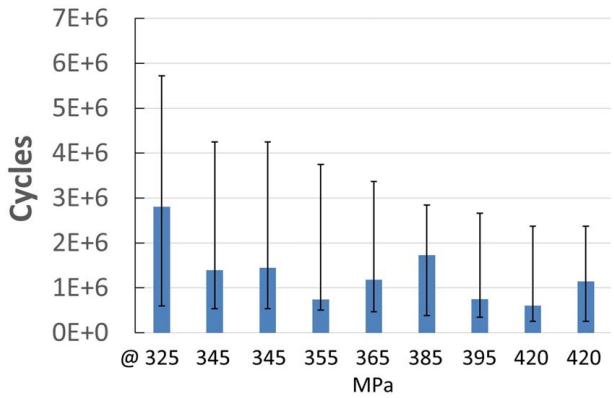

Fig. 12 Comparison of experimental life with prediction interval for different stress amplitudes (horizontal axis compares individual fatigue samples, ordered by increasing stress amplitude)

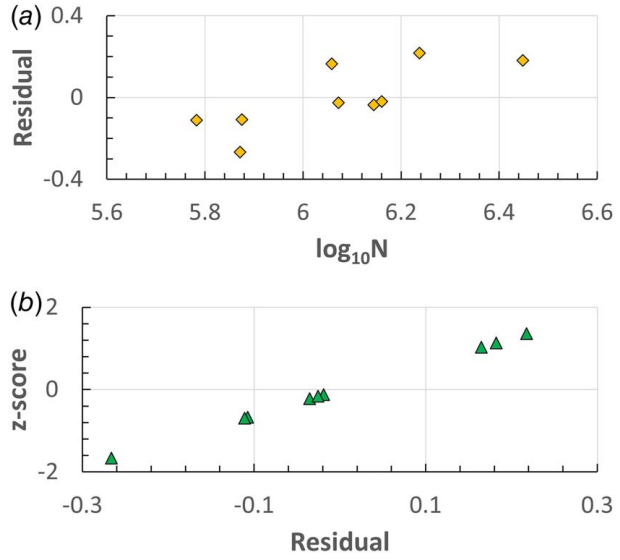

Fig. 13 (*a*) Plot of residual errors from regression and (*b*) normal probability plot of residuals.

Figure 13 shows the two test conditions for applying linear regression to the logarithmic *S-N* data. While the homoscedasticity condition is satisfied by the linear plot of the residual z-scores (Fig. 13(*b*)), the residuals show a possible increasing trend with logarithmic life (Fig. 13(*a*)). Even though a strong number of data points were used, the random scattering makes it difficult to definitively deny the residuals are distributed in a horizontal band that is symmetric about the x-axis. As such, it is assumed that the linear regression assumptions are satisfied.

5 Conclusions

The random geometrical defects inherent to the LPBF process cause the scattering of fatigue life and endurance limit S_e. In this work, an *S-N* curve for LPBFed SS 316L is experimentally constructed to capture the statistical scatter in the fatigue life at different stress amplitudes. Two different runout criteria are tested to investigate any fatigue limit underestimation. The experimental *S-N* curve is normalized using Murakami's lower bound fatigue strength to compare the prediction to the experimentally found endurance limit. In addition, the fatigue scattering is quantified by using 95% prediction intervals for the lower and upper bounds finite fatigue life. The following key points have been made:

- Sufficient testing at a dependable runout criterion (1×10^7 cycles) and testing lightly at a stricter runout criterion (2×10^7 cycles) capture the scattering nature near the knee point.

- The endurance limit of the LPBF SS 316L material is about 300 MPa for the process parameters and resulting defect size distribution.
- The defect-based model predicted endurance limit is lower than the experimental endurance limit, which can either be taken as a conservative measure or an underprediction.
- The upper bound fatigue life at 95% probability is much further from the population mean value than the lower bound fatigue life ($\sim 10^6$ cycles versus $\sim 10^5$ cycles).

Funding Data

- National Science Foundation (Grant Nos. CMMI-2152908 and CMMI-2323083).

Conflict of Interest

There are no conflicts of interest.

Data Availability Statement

The datasets generated and supporting the findings of this article are obtainable from the corresponding author upon reasonable request.

References

[1] Murakami, Y., Takagi, T., Wada, K., and Matsunaga, H., 2021, "Essential Structure of S-N Curve: Prediction of Fatigue Life and Fatigue Limit of Defective Materials and Nature of Scatter," Int. J. Fatigue, **146**, p. 106138.

[2] Shrestha, R., Simsiriwong, J., and Shamsaei, N., 2021, "Fatigue Behavior of Additive Manufactured 316L Stainless Steel Under Axial Versus Rotating-Bending Loading: Synergistic Effects of Stress Gradient, Surface Roughness, and Volumetric Defects," Int. J. Fatigue, **144**, p. 106063.

[3] Tang, M., and Pistorius, P. C., 2017, "Oxides, Porosity and Fatigue Performance of AlSi10Mg Parts Produced by Selective Laser Melting," Int. J. Fatigue, **94**, pp. 192–201.

[4] Liverani, E., Toschi, S., Ceschini, L., and Fortunato, A., 2017, "Effect of Selective Laser Melting (SLM) Process Parameters on Microstructure and Mechanical Properties of 316L Austenitic Stainless Steel," J. Mater. Process. Technol., **249**, pp. 255–263.

[5] Gordon, J. V., Narra, S. P., Cunningham, R. W., Liu, H., Chen, H., Suter, R. M., Beuth, J. L., and Rollett, A. D., 2020, "Defect Structure Process Maps for Laser Powder Bed Fusion Additive Manufacturing," Addit. Manuf., **36**, p. 101552.

[6] Smoqi, Z., Gaikwad, A., Bevans, B., Kobir, M. H., Craig, J., Abul-Haj, A., Peralta, A., and Rao, P., 2022, "Monitoring and Prediction of Porosity in Laser Powder Bed Fusion Using Physics-Informed Meltpool Signatures and Machine Learning," J. Mater. Process. Technol., **304**, p. 117550.

[7] Mohr, G., Altenburg, S. J., Ulbricht, A., Heinrich, P., Baum, D., Maierhofer, C., and Hilgenberg, K., 2020, "In-Situ Defect Detection in Laser Powder Bed Fusion by Using Thermography and Optical Tomography—Comparison to Computed Tomography," Metals (Basel), **10**(1), p. 103.

[8] Murakami, Y., 1994, "Inclusion Rating by Statistics of Extreme Values and Its Application to Fatigue Strength Prediction and Quality Control of Materials," J. Res. Nat. Inst. Stand. Technol., **99**(4), pp. 345–351.

[9] Murakami, Y., 2002, *Metal Fatigue: Effects of Small Defects and Nonmetallic Inclusions*, Elsevier Science Ltd., Amsterdam, Netherlands.

[10] Murakami, Y., Kodoma, S., and Konuma, S., 1989, "Quantitative Evaluation of Effects of Non-Metallic Inclusions on Fatigue Strength of High Strength Steels. I: Basic Fatigue Mechanism and Evaluation of Correlation Between the Fatigue Fracture Stress and the Size and Location of Non-Metallic Inclusions," Int. J. Fatigue, **11**(5), pp. 291–298.

[11] Murakami, Y., and Usuki, H., 1989, "Quantitative Evaluation of Effects of Non-Metallic Inclusions on Fatigue Strength of High Strength Steels. II: Fatigue Limit Evaluation Based on Statistics for Extreme Values of Inclusion Size," Int. J. Fatigue, **11**(5), pp. 299–307.

[12] Murakami, Y., Masuo, H., Tanaka, Y., and Nakatani, M., 2019, "Defect Analysis for Additively Manufactured Materials in Fatigue From the Viewpoint of Quality Control and Statistics of Extremes," Procedia Struct. Integrity, **19**, pp. 113–122.

[13] Zhang, M., Sun, C. N., Zhang, X., Goh, P. C., Wei, J., Hardacre, D., and Li, H., 2017, "Fatigue and Fracture Behaviour of Laser Powder Bed Fusion Stainless Steel 316L: Influence of Processing Parameters," Mater. Sci. Eng. A, **703**, pp. 251–261.

[14] Werner, T., Madia, M., and Zerbst, U., 2021, "Comparison of the Fatigue Behavior of Wrought and Additively Manufactured AISI 316L," *Procedia Structural Integrity*, F. Levebvre and P. Souquet, eds., Elsevier B.V., Amsterdam, Netherlands, pp. 554–563.

[15] Elangeswaran, C., Cutolo, A., Muralidharan, G. K., de Formanoir, C., Berto, F., Vanmeensel, K., and Van Hooreweder, B., 2019, "Effect of Post-Treatments on the Fatigue Behaviour of 316L Stainless Steel Manufactured by Laser Powder Bed Fusion," Int. J. Fatigue, **123**, pp. 31–39.

[16] Zhu, W., Moumni, Z., Zhu, J., Zhang, Y., Li, S., and Zhang, W., 2023, "A Multi-Scale Experimental Investigation for Fatigue Limit and Fatigue Crack Initiation Behavior of Powder Bed Fusion-Laser Beam 316L Stainless Steel," Mater. Sci. Eng. A, **866**, p. 144692.

[17] De Finis, R., Palumbo, D., Ancona, F., and Galietti, U., 2015, "Fatigue Limit Evaluation of Various Martensitic Stainless Steels With New Robust Thermographic Data Analysis," Int. J. Fatigue, **74**, pp. 88–96.

[18] ASTM International, 2023, "A473 Standard Specification for Stainless Steel Forgings," ASTM International, West Conshohocken, PA.

[19] ASTM International, 2021, "F2971 Standard Practice for Reporting Data for Test Specimens Prepared by Additive Manufacturing," ASTM International, West Conshohocken, PA.

[20] ASTM International, 2020, "E3166 Standard Guide for Nondestructive Examination of Metal Additively Manufactured Aerospace Parts After Build," ASTM International, West Conshohocken, PA.

[21] ASTM International, 2021, "F2924 Standard Specification for Additive Manufacturing Titanium-6 Aluminum-4 Vanadium With Powder Bed Fusion," ASTM International, West Conshohocken, PA.

[22] Kousoulas, P., and Guo, Y. B., 2023, "Process Signature for Porosity-Dominant Fatigue Scattering of Materials Processed by Laser Fusion," J. Fail. Anal. Prev., **23**(5), pp. 2075–2089.

[23] Kousoulas, P., and Guo, Y. B., 2023, "A Statistics of Extremes-Based Method to Predict the Upper Bound of Geometrical Defects in Powder Bed Fusion," Manuf. Lett., **35**, pp. 80–87.

[24] Kousoulas, P., and Guo, Y. B., 2023, "On the Probabilistic Prediction for Extreme Geometrical Defects Induced by Laser-Based Powder Bed Fusion," CIRP J. Manuf. Sci. Technol., **41**, pp. 124–134.

[25] Cui, L., Jiang, F., Peng, R. L., Mousavian, R. T., Yang, Z., and Moverare, J., 2022, "Dependence of Microstructures on Fatigue Performance of Polycrystals: A Comparative Study of Conventional and Additively Manufactured 316L Stainless Steel," Int. J. Plast., **149**, p. 103172.

[26] Murakami, Y., and Beretta, S., 1999, "Small Defects and Inhomogeneities in Fatigue Strength: Experiments, Models, and Statistical Implications," Extremes (Boston), **2**(2), pp. 123–147.

[27] Mower, T. M., and Long, M. J., 2016, "Mechanical Behavior of Additive Manufactured, Powder-Bed Laser-Fused Materials," Mater. Sci. Eng. A, **651**, pp. 198–213.

[28] Wycisk, E., Solbach, A., Siddique, S., Herzog, D., Walther, F., and Emmelmann, C., 2014, "Effects of Defects in Laser Additive Manufactured Ti-6Al-4V on Fatigue Properties," Phys. Procedia, **56**, pp. 371–378.

[29] Romano, S., Brückner-Foit, A., Brandão, A., Gumpinger, J., Ghidini, T., and Beretta, S., 2018, "Fatigue Properties of AlSi10Mg Obtained by Additive Manufacturing: Defect-Based Modelling and Prediction of Fatigue Strength," Eng. Fract. Mech., **187**, pp. 165–189.

[30] Weiss, N. A., 2020, *Introductory Statistics*, 10th ed., Pearson, Hoboken.